

## HYDRODYNAMICS AND TURBULENCE DYNAMICS UNDER LARGE-SCALE BICHROMATIC BREAKING WAVES

Dominic van der A (1), Joep van der Zanden (2), Bjarke Eltard Larsen (3),  
Pietro Scandura (4) and Ming Li (5)

(1) University of Aberdeen, United Kingdom, E-mail: [d.a.vandera@abdn.ac.uk](mailto:d.a.vandera@abdn.ac.uk)

(2) MARIN, the Netherlands, E-mail: [j.v.d.Zanden@marin.nl](mailto:j.v.d.Zanden@marin.nl)

(3) DTU, Denmark, E-mail: [bjelt@mek.dtu.dk](mailto:bjelt@mek.dtu.dk)

(4) University of Catania, Italy, E-mail: [pietro.scandura@unict.it](mailto:pietro.scandura@unict.it)

(5) University of Liverpool, United Kingdom, E-mail: [M.Li@liverpool.ac.uk](mailto:M.Li@liverpool.ac.uk)

Experiments were conducted in a large-scale wave flume involving a bichromatic wave group breaking over a fixed barred beach profile. Velocity profiles were measured using optical and acoustics instrumentation at 22 cross-shore locations ranging from the shoaling zone to the inner surf zone. The measurements show that turbulence in the shoaling region is primarily bed-generated and decays almost fully within one wave cycle, in contrast, in the surf zone the breaking-generated turbulence, decays over multiple wave cycles, leading to a gradual increase and decay of Turbulent Kinetic Energy (TKE) during a wave group cycle. The measurements are compared to a two-phase RANS model based on a new stabilized  $k-\omega$  turbulence closure. The model accurately predicts the water surface elevation, and outperforms standard non-stabilized model in predicting the undertow profile and TKE levels in the shoaling zone and outer surf zone.

### 1. INTRODUCTION

Predicting cross-shore sediment transport remains a difficult task since the net sediment transport is affected by various hydrodynamic processes such as undertow, wave skewness and asymmetry, and various forms of boundary layer streaming. In the surf zone additional complexities arise from wave breaking-induced turbulence and the horizontal and vertical flow non-uniformities. In many practical applications for predicting cross-shore sediment transport, empirical/semi-empirical transport formulas are coupled with numerical hydrodynamic models based on the non-linear-shallow water (NLSW) equations. These models have difficulties in predicting cross-shore sediment transport, particularly in the surf zone, which can be largely attributed to a limited quantitative understanding of the near-bed hydrodynamics and sediment transport processes in the surf zone.

This study focusses on plunging breaking waves, which are characterized by the forward curling front of the overturning wave, which transforms into a jet that impinges the water surface and invades the water column. Under plunging breakers, breaking-generated turbulence is transported more quickly down to the bed and mixing rates are higher than for spilling breakers, therefore plunging waves may be expected to have a stronger and more direct effect on surf zone sediment transport than spilling breakers. The spatial and temporal distributions of turbulence under plunging waves have been measured extensively in laboratory wave flumes at small scale, mostly over plane-sloping beds (e.g. Ting & Kirby, 1995; De Serio & Mossa, 2006; Govender et al., 2011), and at large scale over barred bed profiles (e.g. Yoon & Cox, 2010; van der A et al., 2017). These studies revealed strong spatial variation with highest turbulent kinetic energy (TKE) in the breaking region near the water surface, from where turbulence spreads vertically and horizontally due to diffusion, wave-related advection, and current-related advection. The flow non-uniformity, in the presence of wave breaking turbulence, can also further enhance turbulence production in the water column (van der Zanden et al., 2018). The time-dependent transport and production rates lead to a strong temporal variation in TKE, with peaks during the wave crest cycle or the wave trough cycle and may take multiple wave cycles for breaking generated turbulence to decay. The magnitude and direction of these transport processes and the timing of peak TKE depend strongly on cross-shore location, breaking process, and bed geometry.

Computational fluid dynamics (CFD) either through a RANS approach or using a LES approach can potentially handle the breaking processes and boundary layer dynamics naturally. Various studies have applied RANS models to reproduce time-varying TKE, as well as spatial distributions of time-averaged TKE at outer flow levels (e.g. Jacobsen et al., 2014) and inside the wave bottom boundary layer (Fernandez-Mora et al., 2016). Although qualitatively successful, RANS approaches report a consistent overestimation of the modelled TKE in the pre-breaking and the wave breaking regions. A recent study by Larsen and Fuhrman (2018) shows how the overestimation of turbulence pre-breaking comes from an instability problem for RANS models when applied to free-surface waves. An improved model that eliminates the problem was analytically derived and numerically tested, showing significant improvements in modelled turbulence levels as well as in undertow profiles in the pre-breaking and initial breaking regions. The main aim of the present project was to study the spatial and temporal distribution under a bichromatic wave group, which resemble better natural waves which tend to arrive in groups, and allows use to study the wave-to-wave variation of turbulence better compared to regular waves. Moreover, using a repeatable wave group enables ensemble averaging to determine the turbulence statistics. The secondary aim of the project was to generate a high-resolution dataset to test the new stabilized RANS model's ability to accurately simulate the hydrodynamics and turbulence under a bichromatic wave group breaking over a barred profile.

## 2. EXPERIMENTAL SET-UP

The experiment were conducted in the 100 m long, 3 m wide and 5 m deep wave flume at the Polytechnic University of Catalonia in Barcelona. The bed profile was generated in a previous experiment (van der A et al., 2017) and consisted of an offshore slope with a breaker bar and trough (Figure 1a). The bed profile was fixed by replacing the top 0.2m layer of sand with a layer of concrete. To increase the bed roughness and ensure that the wave bottom boundary layer was in the rough turbulent regime similar to natural beaches, a single layer of gravel with  $d_{50} = 9.0\text{mm}$  was glued to the concrete bed surface. The experimental conditions involved two wave conditions: a bichromatic condition, with short wave frequency components  $f_1 = 0.25\text{ Hz}$  and  $f_2 = 0.22\text{ Hz}$ , resulting in a wave group with group period  $T_{gr} = 31.5\text{ s}$  that consisted of 7.5 short waves with mean period  $T_m = 4.2\text{ s}$  and maximum wave height at the paddle of  $H = 0.58\text{m}$ , and a regular wave with period  $T = 6\text{ s}$  and  $H = 0.55\text{m}$ . In this paper we focus on the bichromatic wave condition only, results of the regular wave experiment are presented in Scandura et al. (2018).

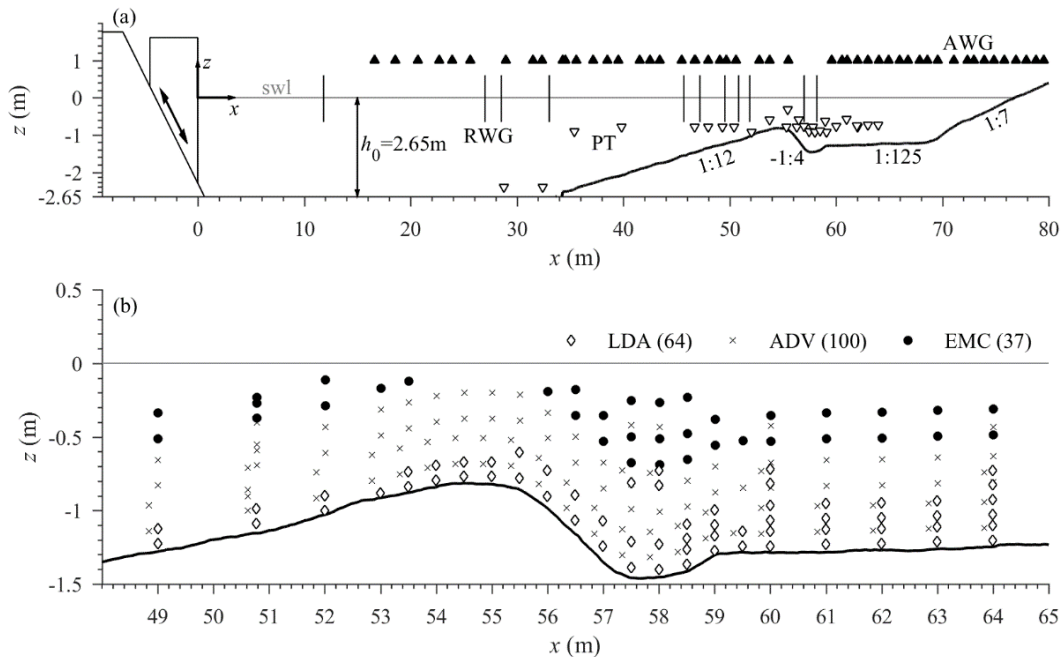


Figure 1. Experimental set-up (a) beach profile including locations of the water surface measurements (RWG = resistive wave gauges; AWG = acoustics wave gauges; PT = pressure transducers); (b) locations of the velocity measurements (LDA = laser Doppler anemometry; ADV = acoustic Doppler Velocimeter; EMC = electromagnetic current meter)

The water surface elevation was measured at a sampling frequency  $f_s = 40$  Hz, with resistive wave gauges (RWGs) at 12 cross-shore locations and with acoustic wave gauges (AWGs) at 52 locations (Figure 1a). In addition, pressure transducer (PT) measurements of the dynamic pressure at 28 cross-shore locations were used to retrieve the water surface level by applying the non-linear weakly dispersive approach by Bonneton et al. (2018). The PTs were primarily deployed in the breaking region, where the RWGs and AWGs suffer from spurious measurements due to bubbles and splash-up of water.

Velocities were measured using two laser Doppler anemometers (LDAs), two acoustic Doppler velocimeters (ADV), and two electromagnetic current meters (ECMs), deployed from a measurement frame attached to a carriage on top of the flume (Figure 2). This “mobile frame” could be repositioned at any elevation (with mm accuracy) and cross-shore location (with cm accuracy). Velocities in cross-shore, transverse and vertical direction are defined  $u$ ,  $v$  and  $w$ , respectively. The LDAs were two identical Dantec two-component backscatter systems, consisting of a 14 mm diameter submersible transducer probe with 50 mm focal length. The instantaneous LDA sampling frequency depends on seeding particle density and flow velocity, but was about  $f_s = 300$  Hz on average for the present experiment. The lower ADV (“ADV1” in what follows) was a side-looking Nortek Vectrino, while the upper ADV (“ADV2” in what follows) was a downward-looking Nortek Vectrino+. The two ADVs measured the three-component velocity at  $f_s = 100$  Hz. The two disc-shaped ECMs, custom-built by Deltares, measured the  $u$  and  $w$  component at  $f_s = 40$  Hz.

The flow velocity was measured at 22 cross-shore locations ranging from  $x = 49$ -64 m. For each cross-shore position, the frame was positioned at three different elevations, which after discarding spurious data resulted in approximately 200 velocity measurement locations (Figure 1b). Additional detailed measurements of the WBL flow were obtained in the shoaling zone  $x = 50.78$  m. These velocities were measured with the LDA at 16 vertical positions, starting from 0.005 m up to 0.125 m from the top of the bed roughness and logarithmically spaced to capture the velocity distribution within the boundary layer. For the regular waves measurements were obtained for a duration of 12 min at each elevation, corresponding to approximately 120 waves, while for the bichromatic waves the measurement duration was 58 min at each elevation, corresponding to approximately 100 wave groups.

Due to the repeatability of the regular waves and the wave groups the phase-averaged quantities could be determined, which enabled decompositions of the velocities into a time-averaged component, a periodic component and the turbulent fluctuation. The periodic component was separated into a low-frequency (long wave) and high-frequency (short wave) component, by separating the signal with a cut-off frequency of 0.1 Hz.

### 3. WATER SURFACE ELEVATION

Time series of the phase-averaged water surface elevation  $\eta$  at three cross-shore locations are shown in Figure 2a-c. To facilitate a good inter-comparison, the time series in these figures were time-referenced such that  $t/T_{gr} = 0$  corresponds to the passage of the front of the group at each location. Note that the grey contours around the lines mark  $\pm$  one standard deviation - the contours are barely visible, which indicates the excellent repeatability of the wave groups.

Figure 2a shows that after generation, the short waves forming the wave group are slightly skewed (crests higher than troughs) and approximately symmetric. As the wave group propagates over the slope, the short waves become higher, more skewed, and more asymmetric (‘sawtooth-shaped’). At  $x = 50.9$  m (Figure 2b), which is in the shoaling region before wave breaking, the wave group consists of seven well-defined short waves. The five highest short waves broke over the bar as plunging-type breakers, with the “plunge point”, i.e. the location where the plunging jet first strikes the water surface, for waves two to six located at  $x = 58.5$ , 57.5, 56.5, 57.5 and 57.5 m, respectively. The first and seventh short waves broke at the shoreline. The “break point” (where the wave starts to overturn) of the most offshore breaking wave was measured at  $x = 54.0$  m, while the “splash point” (where the bounced jet strikes the water surface a second time) of wave two was located at  $x = 60.0$  m. Based on these visual observations we define the shoaling region ( $x < 54$  m), breaking region ( $54 \text{ m} < x < 60$  m), and inner surf zone ( $x > 60$  m). Hence, Figure 3c ( $x = 66.0$  m) corresponds to the inner surf zone

where waves two to six have broken and have transformed into surf bores. These five surf bores have similar wave heights, are highly skewed, and are significantly lower in wave height than at  $x = 50.9$  m.

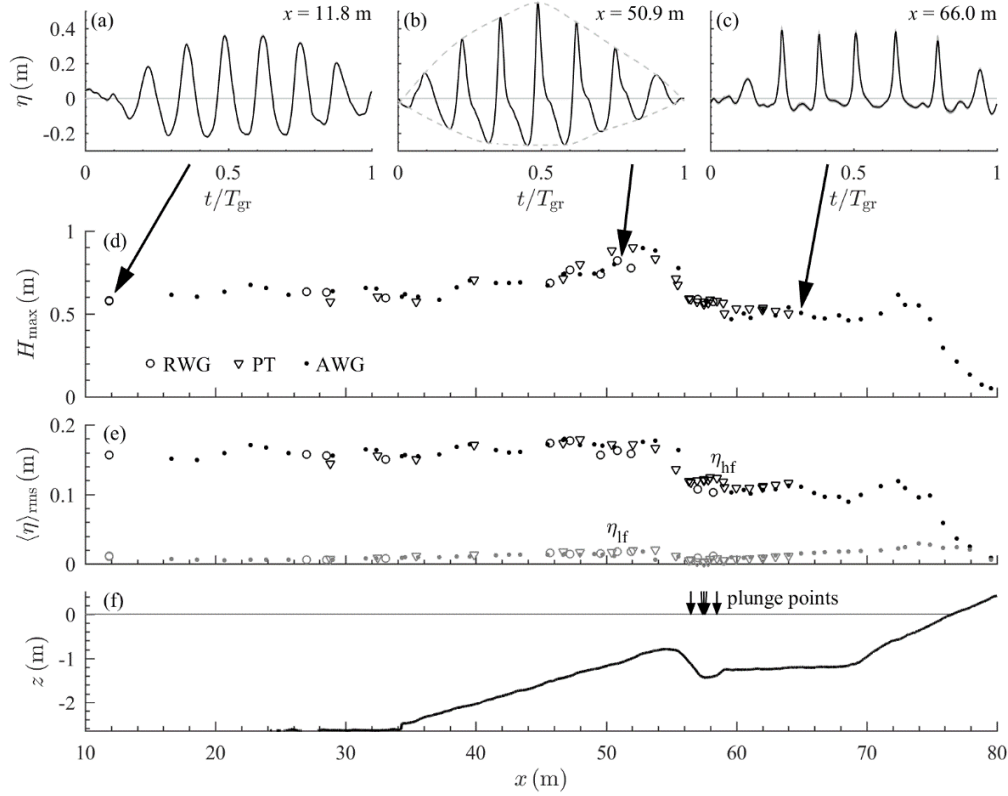


Figure 2. (a-c) Time series of phase-averaged water surface, measured by RWG (a, b) and AWG (c) (solid), with dashed lines in (b) marking the upper and lower bounds of the wave group envelope; (d) Maximum wave height  $H_{max} = \langle \eta \rangle_{max} - \langle \eta \rangle_{min}$ , measured by RWGs (circles), PTs (triangles) and AWGs (dots); (e) Root-mean-square water surface elevation, high-frequency (black symbols) and low-frequency (grey symbols) components; (f) bed profile including locations of the five plunge points.

Figure 2d shows the cross-shore distribution of the maximum wave height  $H_{max} = \langle \eta \rangle_{max} - \langle \eta \rangle_{min}$ . The three instruments yield generally consistent results, although the PTs tend to underestimate the wave height in the breaking region, where waves are strongly skewed and asymmetric, due to strong pressure attenuation of the higher harmonics of the wave. The wave heights are approximately constant over the horizontal, deeper part of the flume ( $x < 34$  m), except for some modulations that are attributed to wave reflection at the beach and at the offshore slope. As waves shoal over the offshore slope, the wave height increases up to  $H_{max} = 0.90$  m at  $x = 52.8$  m. The maximum wave height decreases by about 50% between  $x = 53.8$  m and  $59.6$  m due to wave breaking. Between  $x = 60$  and  $70$  m the wave height remains approximately constant, while over the sloping beach ( $x > 70$  m) the waves shoal and break a second time.

The water surface elevation was decomposed into a high-frequency ( $\eta_{hf}$ ) and low-frequency ( $\eta_{lf}$ ) component. Figure 2e shows the cross-shore distribution of  $\langle \eta \rangle_{rms}$  for both components. It can be seen that  $\langle \eta_{hf} \rangle_{rms}$  is approximately uniform over the offshore slope, which indicates that the increase in  $H_{max}$  (Figure 2b) is primarily due to an increasing skewness of the waves. The low-frequency component  $\langle \eta_{lf} \rangle_{rms}$  gradually increases between the wave paddle and the bar crest, which relates to shoaling of the long wave and to energy transfer from the short waves to the wave group as shown in several other studies. Both  $\langle \eta_{lf} \rangle_{rms}$  and  $\langle \eta_{hf} \rangle_{rms}$  decrease in the wave breaking region around the bar crest ( $x \approx 55.0$  m). Such decrease at both high and low frequencies near the break point is consistent with several other laboratory studies (see Baldock, 2012, for an overview). The low-frequency wave energy increases across the inner surf zone towards the shoreline ( $x = 55$  to  $75$  m) as the wave groups shoal for the second time.

#### 4. FLOW VELOCITIES

Time series of the phase-averaged horizontal and vertical velocities  $\langle u \rangle$  and  $\langle w \rangle$  in the free-stream ( $z - z_{\text{bed}} \approx 0.4$  m) at four cross-shore locations are shown in Figure 3. The time series reveal the strongly skewed-asymmetric shape of the short-wave-induced velocity at all locations. The orbital amplitude increases from  $x = 49.0$  to  $54.0$  m (shoaling region to bar crest). At  $x = 54.0$  m, the highest velocities in both onshore (1.3 m/s) and offshore (-1.1 m/s) direction occur. The orbital amplitude decreases strongly between  $x = 54.0$  and  $58.0$  m (bar crest to trough) due to a combination of wave energy dissipation and an increasing water depth. At the same time the magnitude of the undertow increases, leading to increasing durations of the negative (seaward-directed) flow half cycles. At  $x = 62.0$  m the undertow has weakened and the duration of the positive (shoreward-directed) flow half cycles increases again.

Figure 3 further includes the low-frequency velocity  $\langle \tilde{u}_{\text{lf}} \rangle$  (dashed lines). The amplitude of the low-frequency velocity shows a clear variation with cross-shore location. The amplitude of  $\langle \tilde{u}_{\text{lf}} \rangle$  is small in the shoaling region (e.g.  $x = 49.0$  m), but its magnitude increases in the breaking region at the bar crest ( $x = 54.0$  m) and reaches a maximum at  $x = 58.0$  m, which corresponds to the bar trough and is located about 1 m shoreward from the plunge point of the largest breaking waves. At  $x = 62.0$  m, the amplitude of  $\langle \tilde{u}_{\text{lf}} \rangle$  has decreased again. This cross-shore variation of  $\langle \tilde{u}_{\text{lf}} \rangle_{\text{rms}}(x)$  differs from the variation of  $\langle \eta_{\text{lf}} \rangle_{\text{rms}}(x)$  (Figure 3e), which indicates that the low-frequency velocity variations are not directly driven by the water surface level variations at the wave group frequency. Instead, the large  $\langle \tilde{u}_{\text{lf}} \rangle$  values for  $x = 57 - 59.5$  m are explained by time variations in the return flow induced by the successive breaking waves: the return flow, averaged over a short wave cycle, is relatively low under the non-breaking waves and relatively high under the highest breaking waves, hence yielding a periodic velocity oscillation at the wave group time scale (see also, e.g., Alsina and Caceres, 2011). The  $\langle \tilde{u}_{\text{lf}} \rangle$  oscillations in the surf zone can thus be interpreted as a wave to wave variation in “undertow” velocity, although it should be stressed that the term “undertow” is used in the present study for the longer-term (i.e., wave-group-averaged), and not for the short-wave-averaged, cross-shore velocity.

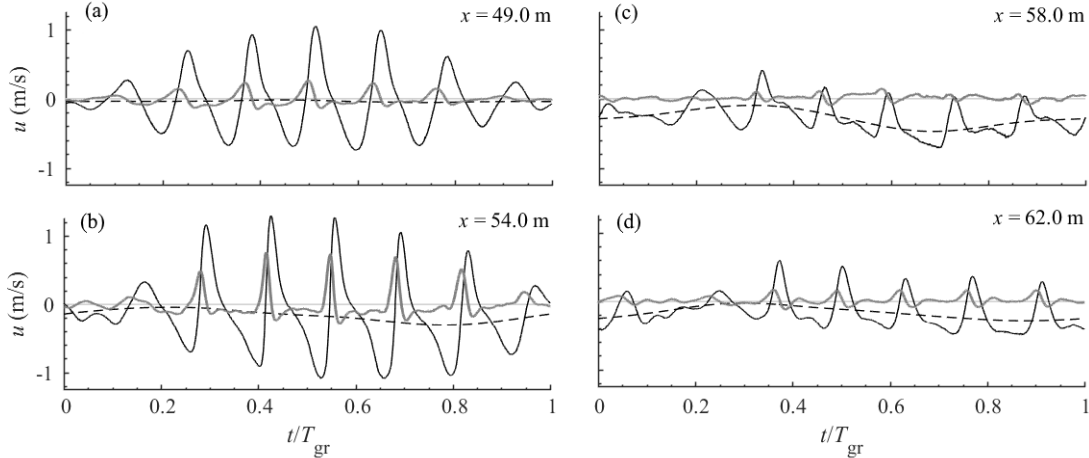


Figure 3. Time series of phase-averaged velocities  $\langle u \rangle$  (solid black),  $\langle \tilde{u}_{\text{lf}} \rangle + \bar{u}$  (dashed black), and  $\langle w \rangle$  (solid grey) at eight locations and at  $z - z_{\text{bed}} \approx 0.40$  m.

The spatial distribution of the time-averaged cross-shore velocity  $\bar{u}$  is shown in Figure 4. The time-averaged cross-shore velocity magnitude increases from -0.05 m/s in the shoaling region to a maximum of -0.3 m/s in the breaking region over the bar trough, followed by a decrease to -0.2 m/s in the inner surf zone. Mass continuity requires these cross-shore variations in time-averaged cross-shore velocity to be balanced by a time-averaged velocity in vertical direction ( $d\bar{u}/dx = -d\bar{w}/dz$ ), which the measurements do indeed confirm (not shown for brevity).

The undertow profiles in Figure 4 differ strongly in shape: around the bar crest ( $x = 53$  to  $56$  m, i.e. under wave break points)  $\bar{u}(z)$  distributions tend to convex shapes, while  $\bar{u}(z)$  over the bar trough ( $x = 58$  to  $61$  m, i.e. under splash points) increases strongly within the first few cm above the bed and tends to a concave shape at higher elevations. The variation of these undertow shapes, and their spatial occurrence relative to break and splash points, is consistent with



previous observations of regular (e.g. Govender et al., 2011) and irregular (Boers, 2005) breaking waves over a bar.

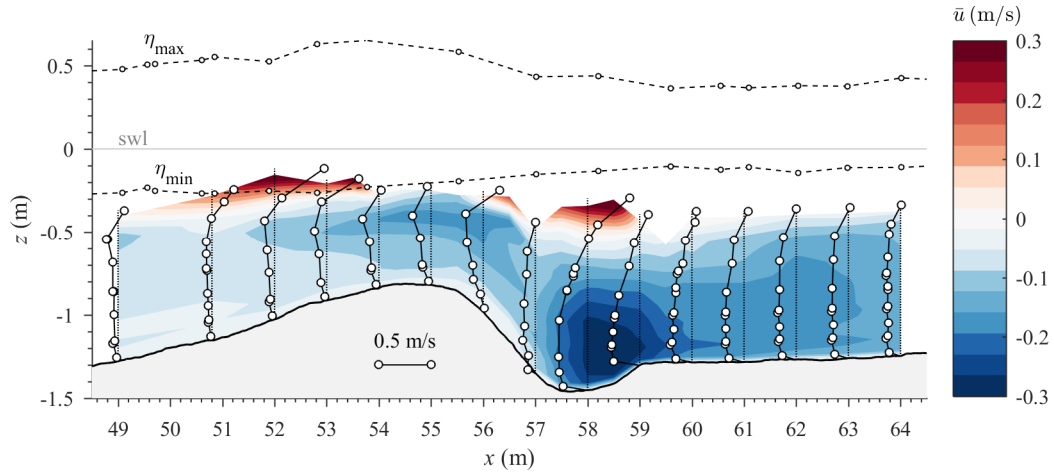


Figure 4. Spatial distribution of time-averaged cross-shore velocity  $\bar{u}$ .

## 5. TURBULENCE

Figure 5 shows time series of phase-averaged TKE,  $\langle k \rangle$ , at four cross-shore locations and at two elevations:  $z - z_{bed} = 0.40$  m (free-stream) and  $0.025$  m (in the WBL). In the shoaling region at  $x = 49.0$  m  $\langle k \rangle$  shows pairs of short-duration peaks within the boundary layer (Figure 5b, grey line), that lag the maximum offshore- and onshore-directed velocity by approximately  $0.2T_m$  (Figure 5a). These TKE peaks relate to turbulence that is produced at the bed during each half-cycle and that subsequently spreads upward. During the relatively long interval between the maximum onshore and maximum offshore velocity, i.e. under the rear side of the wave,  $\langle k \rangle$  decays to nearly zero until the maximum velocity in offshore direction is reached and the process repeats as described.

At the bar crest ( $x = 55.0$  m), near-bed  $\langle k \rangle$  shows six well-defined peaks that are approximately in phase with the maximum onshore free-stream velocity (Figure 5c,d). The fact that only one peak in  $\langle k \rangle$  appears per wave cycle, instead of two peaks such as at  $x = 49.0$  m, can be explained by the increased wave asymmetry, leading to a shorter time interval between the maximum offshore and maximum onshore velocity and which merges the turbulence peaks into one peak. At the same location at  $z - z_{bed} = 0.40$  m (Figure 5d, black line),  $\langle k \rangle$  is substantially higher than at  $x = 49.0$  m (same elevation) which can be explained by wave breaking turbulence that is advected in offshore direction by the undertow.

Figure 5f shows  $\langle k \rangle$  over the bar trough ( $x = 59.0$  m). At this location  $\langle k \rangle$  is continuously higher at  $z - z_{bed} = 0.40$  m than at  $0.025$  m, due to the injection of turbulence from the breaking waves. The TKE does not dissipate within one wave cycle, leading to a gradual build-up of TKE during the wave group cycle ( $t/T_{gr} = 0.50$  to  $0.80$ ). Consequently,  $\langle k \rangle$  shows a pronounced asymmetry at wave group time scale, with substantially higher TKE under the last three waves in the group ( $t/T_{gr} = 0.75$  to  $0.05$ ) than under the first three waves ( $t/T_{gr} = 0.20$  to  $0.50$ ). Three evident peaks in  $\langle k \rangle$  are observed at  $t/T_{gr} \approx 0.65, 0.80$ , and  $0.90$ . These peaks occur consistently under the rear of the short waves, i.e. around crest to trough reversal, when orbital velocities are downward-directed. Therefore, the occurrence of the peaks in  $\langle k \rangle$  likely relates to an advective influx of TKE by the combined downward-directed time-averaged and periodic velocity.  $\langle k \rangle$  is maximum at  $t/T_{gr} \approx 0.8$ , shortly after the fifth short wave in the wave group has passed. Note that the highest wave upon breaking is the fourth wave (passing  $x = 59.0$  m at  $t/T_{gr} = 0.6$ ) and the maximum  $\langle k \rangle$  thus lags this wave by about 1.5 short wave cycle. Near the bed (grey line)  $\langle k \rangle$  shows a similar time variation at wave group scale, although less pronounced than at  $0.40$  m. Finally, Figure 5h shows the time series of  $\langle k \rangle$  in the inner surf zone ( $x = 64.0$  m), showing that TKE at both elevations is continuously small with minor temporal variation at short-wave and wave-group time scales.

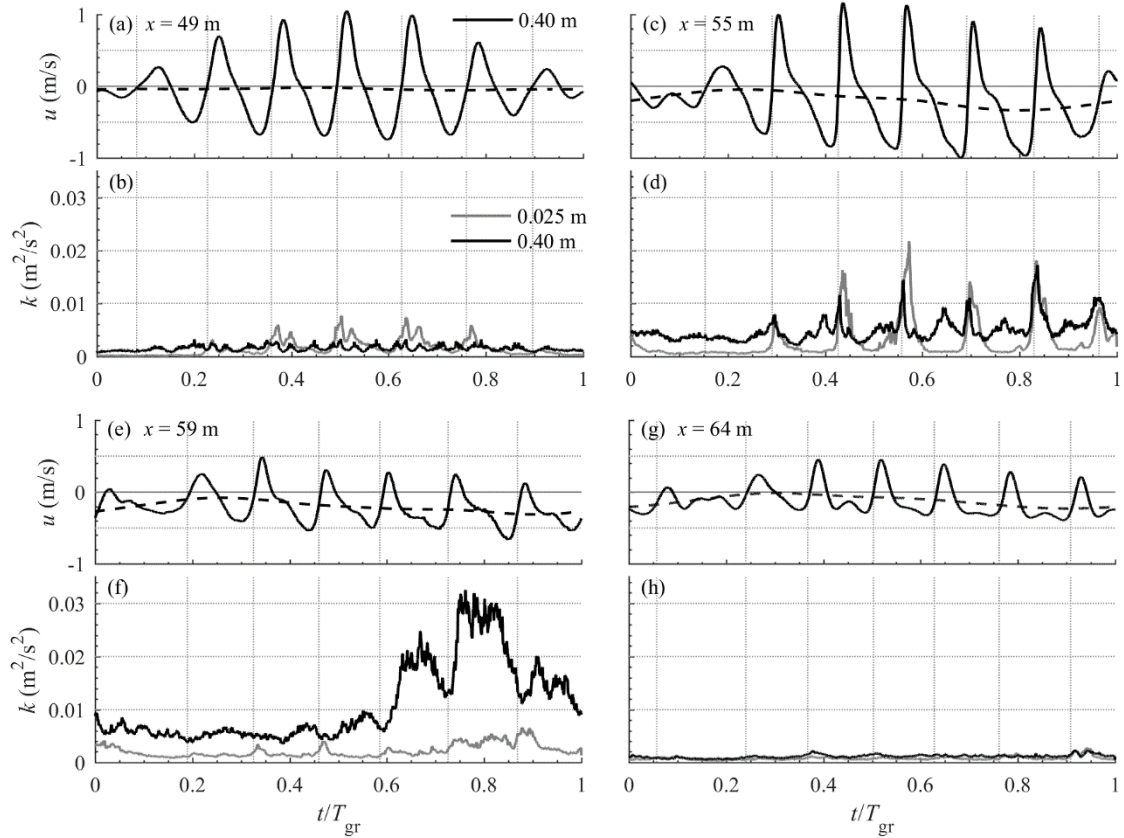


Figure 5. Time series of phase-averaged velocity and TKE at  $x = 49.0$  (shoaling region),  $55.0$  m (bar crest),  $59.0$  m (bar trough), and  $64.0$  m (inner surf zone). (a, c, e, g) Cross-shore velocity  $\langle u \rangle$  (solid) and  $\langle \tilde{u}_{if} \rangle + \bar{u}$  (dashed) at  $z - z_{bed} \approx 0.40$  m; (b, d, f, h) TKE at  $z - z_{bed} \approx 0.40$  m (black) and at  $z - z_{bed} = 0.025$  m (grey). The vertical grid lines mark the zero-up crossings of  $\langle \tilde{u}_{if} \rangle$  at  $z - z_{bed} = 0.40$  m at each location.

## 6. NUMERICAL MODELLING

The simulations are performed using the two-phase volume-of-fluid (VOF) model *waves2foam* developed by Jacobsen et al. (2012), using the new stabilized  $k-\omega$  turbulence closure model described by Larsen & Fuhrman (2018). The simulations are performed in two dimensions, on a bathymetry following grid composed of  $2250 \times 188$  points ( $x$  and  $z$  direction), resulting in 423,000 cells in total. Wave generation is based on a second order bichromatic bidirectional solution, with amplitudes chosen to match the maximum experimental wave height in the flat part of the domain. In total 20 wave groups were simulated and the last 10 groups used to phase-average the model results.

Figure 6a shows the measured and modelled maximum and minimum phase-averaged surface elevations along the flume. The model captures both the highest crest and trough levels in the flat part of the flume ( $x < 34$  m) and during shoaling ( $x \approx 34$  m -  $53$  m). The model accurately captures the point where the wave heights decrease due to breaking ( $x \approx 53$  m). In the inner surf-zone ( $x > 60$  m) crest heights are slightly overestimated, compared to the AWG measurements, but this might be due to the applied de-spiking routine that slightly smoothens the wave crests, as also mentioned by van der Zanden et al. (2019). Closer to the swash zone the second decay in wave height is also captured. The largest difference between the modelled results and the experiments can be seen in the swash zone where the modelled results show an additional small peak. This peak comes from the splash up of one of the waves in the group breaking a second time in the swash zone. In the experiments the waves also shoaled and broke again in the swash zone, but a distinct splash-up as in the model was not measured.

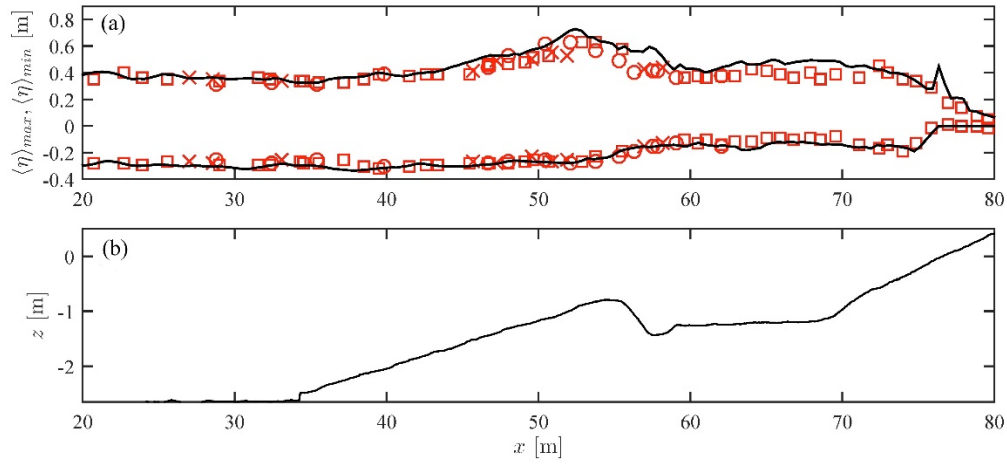


Figure 6. (a) Comparison between measured and modelled water surface envelope; (b) beach profile

Figure 7 shows the spatial distribution of the time-averaged cross-shore velocity (the undertow) of both the model (small circles and colored velocities) and the experiments (large circles). For reference, the figure also includes the results from using a standard non-stabilized two-equation turbulence model (green lines). The experiments showed two distinct different undertow profile shapes in the shoaling region and the surf zone. In the shoaling region ( $x < 56$  m) the magnitude of the undertow is largest far away from the bed, whereas in the surf zone ( $x > 58$  m) the undertow is strongest near the bed. This qualitative difference in the undertow profile as well as the transition in profile shape from one region to the other is well captured by the model. The non-stabilized turbulence model, on the other hand, does not capture the difference in profile shape nor the transition in the shape of the undertow structure between  $x = 56 - 58$  m and instead, returns a similar profile shape from shoaling to inner surf zone. In Larsen and Fuhrman (2018) this behaviour was attributed to the overproduction of turbulence in the pre-breaking region which increases the flow resistance in the upper part of the flow and forces the undertow to maintain the same shape as in the surf zone.

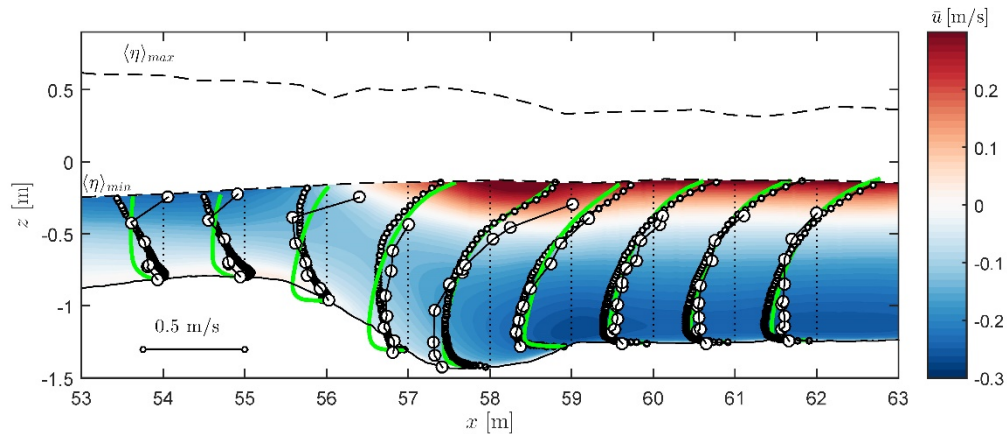


Figure 7. Spatial distribution of the time-averaged cross-shore velocity of the experiments (large circles), from the model (small circles and colored velocities) and using a non-stabilized model (green lines)

The overproduction of turbulence is illustrated in Figure 8, which presents a comparison of the measured time-averaged TKE with the model results based on the new model (Figure 8a) and based on the non-stabilized  $k-\omega$  turbulence closure (Figure 8b). Using a formally stabilized turbulence model, the TKE levels at shoaling and wave breaking locations ( $x = 50.7 - 56$  m) are generally low and correspond well with the measured TKE (Figure 8a). In contrast, using a non-stabilized  $k-\omega$  turbulence model (Figure 8b) yields TKE levels in these regions that are of similar magnitude as in the surf-zone and that are several orders of magnitude larger than the measured levels. In the inner surf zone both the stabilized and non-stabilized model show an overestimation of the TKE. The overestimation is significantly larger for the non-stabilized model which can be explained by the wave arriving at the surf-zone with severely over-estimated turbulence levels, hence advecting additional turbulence into the surf zone.



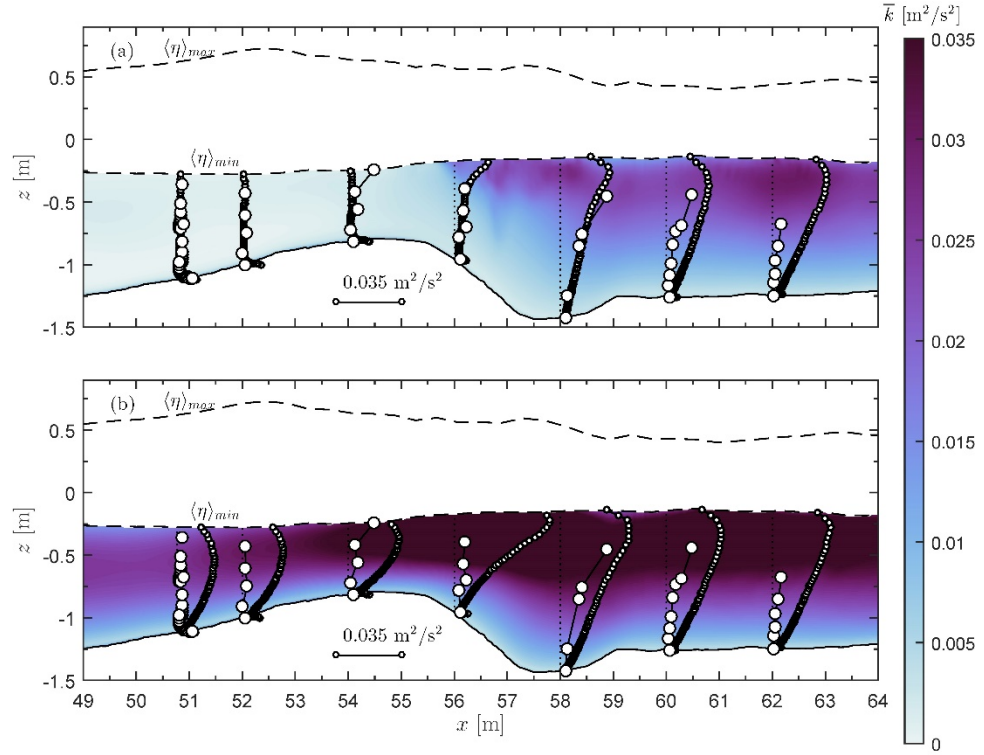


Figure 8. Snapshot of the spatial distribution of TKE upon wave breaking using (a) a formally stable turbulence model and (b) a standard two-equation turbulence model.

## 7. CONCLUSION

Velocity and turbulence profiles were measured under a bichromatic plunging breaking wave in a large-scale wave flume over a fixed barred profile. The measurements covered 22 cross-shore locations that covered part of the shoaling region, the full wave breaking region, and part of the inner surf zone. The bichromatic wave produced a wave group with seven incident short waves, of which the highest five waves were plunging breaking over the bar.

The temporal dynamics of TKE vary strongly across the profile. In the shoaling region, where turbulence is primarily bed-shear generated, turbulence decays within one wave cycle, leading to time-varying TKE at the short wave frequency. In contrast, the wave breaking-generated turbulence between plunge and splash points requires multiple wave cycles to decay fully, leading to a gradual increase in TKE during the group and to variations of TKE at the wave group frequency.

The measurements are compared to a two-phase RANS model based on a new stabilized  $k-\omega$  turbulence closure. Very good agreement is obtained between measured and modelled water surface elevations, meaning that the model handles the wave propagation, shoaling and breaking of the wave group. The model predicts the undertow well and captures the correct shape of the undertow profile and the shape transition between shoaling and surf zone. Standard non-stabilized RANS models are unable to capture this shape transition, due to the inherent overestimation of turbulence in the shoaling zone. The present model still overestimates TKE levels and undertow magnitude in the inner surf zone, similar to many other RANS models, which will be the focus of future research.

## ACKNOWLEDGEMENT

We gratefully acknowledge the CIEMLab team, Iván Cáceres, Andrea Marzeddu, Joaquim Sospedra, and Oscar Galego, for their help during experiments. We also wish to thank all other HYBRID members (Carmelo Petrotta, Carla Faraci, James Cooper, Simon Clark, Stefan Carstensen, David Fuhrman, Stuart McLelland, Guillaume Fromant, David Hurther, Gerben Ruessink, Joost Brinkkemper) for their help during the various stages of the project. BEL acknowledges financial support from the Independent Research Fund Denmark project

SWASH: Simulating WAVE Surf-zone Hydrodynamics and sea bed morphology, Grant no. 8022-00137B. We are grateful to Deltares for lending out their ECMs and to Dr Jose Alsina for his contributions to the generation of the wave paddle steering signals. This project has received funding from the European Union's Horizon 2020 research and innovation programme under grant agreement No 654110, HYDRALAB+.

## REFERENCES

- Alsina, J. M., and Cáceres, I. (2011). Sediment suspension events in the inner surf and swash zone. Measurements in large-scale and high-energy wave conditions. *Coastal Engineering*, 58(8), 657-670.
- Baldock, T. E. (2012). Dissipation of incident forced long waves in the surf zone—Implications for the concept of “bound” wave release at short wave breaking. *Coastal Engineering*, 60, 276-285.
- Bonneton, P., Lannes, D., Martins, K., and Michallet, H. (2018). A nonlinear weakly dispersive method for recovering the elevation of irrotational surface waves from pressure measurements. *Coastal Engineering*, 138, 1-8.
- De Serio, F., and Mossa, M. (2006). Experimental study on the hydrodynamics of regular breaking waves. *Coastal Engineering*, 53(1), 99-113.
- Fernandez-Mora, A., Ribberink, J. S., van der Zanden, J., van der Werf, J. J., and Jacobsen, N. G. (2016). RANS-VOF modeling of hydrodynamics and sand transport under full-scale non-breaking and breaking waves. *Proceedings of the 35th ICCE*, Antalya, Turkey.
- Govender, K., Michallet, H., and Alport, M. J. (2011). DCIV measurements of flow fields and turbulence in waves breaking over a bar. *European Journal of Mechanics B-Fluids*, 30(6), 616-623.
- Jacobsen, N. G., Fuhrman, D. R., and Fredsøe, J., 2012. A wave generation toolbox for the open-source CFD library: OpenFOAM (R). *Int. J. Numer. Meth. Fluids*, 70, 1073–1088.
- Larsen, B. E., and Fuhrman, D. R. (2018). On the over-production of turbulence beneath surface waves in Reynolds-averaged Navier–Stokes models. *Journal of Fluid Mechanics*, 853, 419-460.
- Scandura, P., van der A, D.A., van der Zanden, J., Petrotta, C., Faraci, C., Cooper, J., Clark, S., Eltard Larsen, B., Carstensen, S., Fuhrman, D.R., Cáceres, I., McLellands, S., Fromant, G., Hurther, D., Ruessink, G., Brinkkemper, J., Li, M. (2018). Hydrodynamics under large-scale breaking waves over a barred beach. *Poc. 7<sup>th</sup> Coastlab Conference*, Santander, Spain.
- Ting, F. C. K., and Kirby, J. T. (1995). Dynamics of surf-zone turbulence in a strong plunging breaker. *Coastal Engineering*, 24(3-4), 177-204.
- van der A, D. A., van der Zanden, J., O'Donoghue, T., Hurther, D., Cáceres, I., McLelland, S. J., and Ribberink, J. S. (2017). Large-scale laboratory study of breaking wave hydrodynamics over a fixed bar. *Journal of Geophysical Research: Oceans*, 122(4), 3287-3310.
- van der Zanden, J., van der A, D. A., Cáceres, I., Hurther, D., McLelland, S. J., Ribberink, J. S., and O'Donoghue, T. (2018). Near-bed turbulent kinetic energy budget under a large-scale plunging breaking wave over a fixed bar. *Journal of Geophysical Research: Oceans*, 123(2), 1429-1456.
- van der Zanden, J., van der A, D. A., Cáceres, I., Eltard Larsen, B., Fromant, G., Petrotta, C., Scandura, P., and Li, M. (2019). Spatial and temporal distributions of turbulence under bichromatic breaking waves, *Coastal Engineering*, 146, 65-80.
- Yoon, H. D., and Cox, D. T. (2010). Large-scale laboratory observations of wave breaking turbulence over an evolving beach. *Journal of Geophysical Research-Oceans*, 115.